Annual Methodological Archive Research Review
http://amresearchreview.com/index.php/Journal/about
Volume 3, Issue 9 (2025)

Online ISSN 3007-3197
Print ISSN 3007-3189

http://amresearchreview.com/index.php/Journal/about

TAILORING THE PHOTOPHYSICAL PROPERTIES OF PHOSPHORESCENT $CsPbBr_3$ QUANTAM DOTS VIA TRIAZINE LIGAND FUNCTIONALIZATION

Nadia Afzal
Faculty of Sciences, The Superior University Lahore, Pakistan.

Muhammad Qaiser Zakaria
Institute of Quantum Machanics, Shanghai University Shanghai 200444 China
Department of Physics the University of Lahore Sargodha Campus Punjab Pakistan

Muhammad Atif* (Corresponding author)
Faculty of Sciences, the Superior University Lahore, Pakistan
Email: muhammad.atif.fsd@superior.edu.pk

Amin Masih
Faculty of Sciences, the Superior University Lahore, Pakistan

Rabia Faridi
Department of Plant Breeding and Genetics, University of Agriculture Faisalabad, 38000. Pakistan

Amber Iqbal
Faculty of Sciences, the Superior University Lahore, Pakistan

ABSTRACT

This study investigates the impact of triazine ligand functionalization on the photophysical properties of cesium lead bromide ($CsPbBr_3$) nanocrystals with the aim of enhancing their emission efficiency and stability. Doped $CsPbBr_3$ nanocrystals often suffer from surface trap states that promote non-radiative recombination and reduce photoluminescence performance. By introducing triazine ligands onto the nanocrystal surface, the passivation of these trap states was achieved, resulting in improved exciton stabilization, enhanced radiative recombination, and suppression of non-radiative decay. Steady-state and time-resolved photoluminescence measurements revealed a significant increase in emission intensity and prolonged carrier lifetime, accompanied by a reduction in trap-assisted processes. The functionalized nanocrystals exhibited higher quantum efficiency and greater optical stability compared to their doped counterparts, indicating successful surface modification. These results highlight the potential of triazine functionalization as a rational approach to optimize the optical behavior of halide perovskite nanocrystals, thereby broadening their applicability in optoelectronic devices such as light-emitting diodes, photocatalysts, and solar energy harvesting systems.

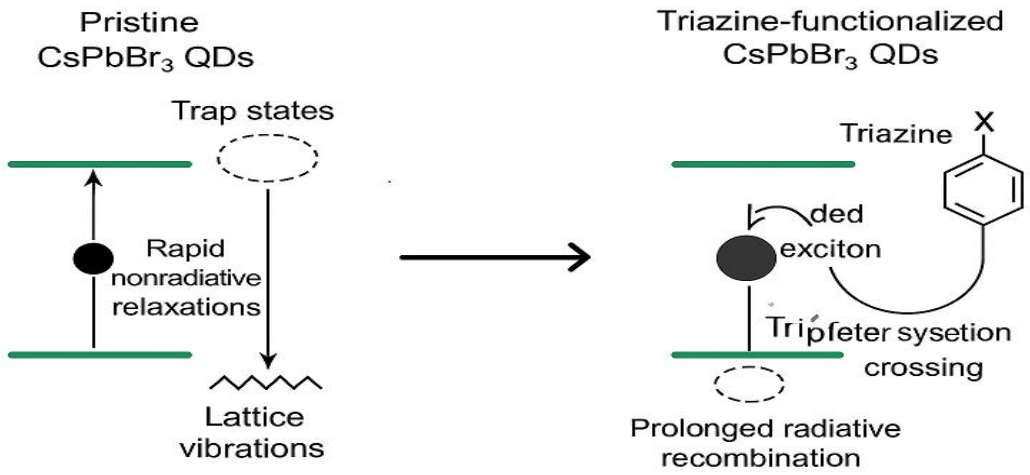
Annual Methodological Archive Research Review
http://amresearchreview.com/index.php/Journal/about
Volume 3, Issue 9 (2025)

Online ISSN 3007-3197
Print ISSN 3007-3189

http://amresearchreview.com/index.php/Journal/about

Keywords: Cspbbr$_3$ Nanocrystals, Triazine Ligand, Surface Passivation, Photoluminescence Enhancement, Exciton Stabilization, Quantum Efficiency, Optical Stability, Optoelectronic Applications

Figure 1: Graphical abstract



1. INTRODUCTION

All-inorganic lead halide perovskites, particularly cesium lead bromide ($CsPbBr_3$), have emerged as promising candidates for optoelectronic and photonic technologies owing to their high absorption coefficients, tunable band gaps, sharp emission linewidths, and high photoluminescence quantum yields (PLQY)[1]. These properties have driven advances in light-emitting diodes, solar cells, lasers, and photodetectors. However, while prompt photoluminescence in $CsPbBr_3$ nanocrystals has been extensively studied, their long-lived photophosphorescence remains underexplored. Efficient afterglow emission is critical for applications such as persistent displays, bioimaging, photocatalysis, data storage, and security tagging, yet it is hindered by surface defects, ionic migration, and dynamic lattice instabilities that promote nonradiative recombination[2]. Surface functionalization has emerged as an effective strategy to mitigate these challenges by modulating surface chemistry and exciton dynamics[3]. In particular, triazine-based ligands present unique advantages due to their conjugated, electron-withdrawing structure, which enables strong Pb–N coordination, suppression of trap states, and stabilization of excitons. Halogen-substituted triazines further enhance spin–orbit coupling, promoting intersystem crossing (ISC) from singlet to triplet states and enriching the population of long-lived excitons responsible for phosphorescence[4]. Beyond defect passivation, the rigid aromatic backbone of triazine ligands provides steric and environmental stability, while

Annual Methodological Archive Research Review
http://amresearchreview.com/index.php/Journal/about
Volume 3, Issue 9 (2025)

Online ISSN 3007-3197
Print ISSN 3007-3189
http://amresearchreview.com/index.php/Journal/about

electronic delocalization at the nanocrystal–ligand interface introduces new radiative recombination channels.

Despite these promising attributes, the role of triazine functionalization in tailoring the exciton relaxation dynamics and persistent luminescence of $CsPbBr_3$ nanocrystals remains insufficiently understood[5]. Addressing this gap is critical for establishing design principles for stable, efficient, and tunable phosphorescent perovskite nanomaterials. This study therefore investigates how triazine ligands influence surface passivation, exciton relaxation pathways, and photophosphorescence in $CsPbBr_3$ quantum dots, aiming to provide mechanistic insights into ligand–nanocrystal interactions that can guide the development of next-generation phosphorescent devices.

2. EXPERIMENTAL

2.1 Synthesis of Triazine doped $CsPbBr_3$ Nanocrystals

$CsPbBr_3$ nanocrystals were synthesized using a modified hot-injection method under an inert nitrogen atmosphere. A cesium oleate precursor was prepared by dissolving cesium carbonate in oleic acid and octadecene at elevated temperature[6]. In a separate three-neck flask, $PbBr_2$ was dissolved in octadecene with oleic acid and oleylamine, and the solution was heated to 160–180 °C. At this stage, the pre-prepared cesium oleate solution was rapidly injected, initiating nucleation and growth of $CsPbBr_3$ nanocrystals. The reaction was quenched after a controlled duration by removing the heating mantle and cooling with an ice-water bath to suppress overgrowth and aggregation. The nanocrystals were precipitated with ethanol, centrifuged, and redispersed in anhydrous toluene for further use[7].

For ligand exchange, triazine and halogen-substituted triazine derivatives were dissolved in toluene at controlled concentrations. The ligand solution was added to $CsPbBr_3$ dispersions and stirred under nitrogen at room temperature, enabling replacement of native oleic acid/oleylamine ligands with triazine-based ligands through Pb–N coordination. Reaction conditions (time, ligand concentration) were optimized to avoid destabilization of the colloidal suspension. The functionalized nanocrystals were purified by precipitation with methyl acetate, centrifugation, and redispersion in toluene. This purification cycle was repeated twice to remove excess ligands and residual organics [8].

2.3 Optical Characterization

Steady-state optical absorption was recorded using UV–Vis spectroscopy, and the optical band gap was determined using Tauc analysis for a direct allowed transition, by extrapolating the linear region of the $(\alpha h\nu)^2$ versus $h\nu$ plot[9]. Photoluminescence (PL) spectra were obtained under identical conditions for all samples to compare peak position, full width at half maximum (FWHM), and integrated intensity. Absolute photoluminescence quantum yields (PLQY) were measured with an integrating sphere[10]. Time-resolved photoluminescence (TRPL) was conducted using pulsed laser excitation and time-correlated single-photon counting. Decay profiles were fitted to multi-exponential functions, and the intensity-weighted average lifetimes were

Annual Methodological Archive Research Review
http://amresearchreview.com/index.php/Journal/about
Volume 3, Issue 9 (2025)

Online ISSN 3007-3197
Print ISSN 3007-3189

http://amresearchreview.com/index.php/Journal/about

calculated. Delayed emission spectroscopy was performed with time-gated detection to probe long-lived photophosphorescence, while low-temperature PL (down to 77 K) was used to distinguish thermally activated quenching from intrinsic long-lived states[11]. Power-dependent PL was measured to evaluate exciton–exciton and trap-mediated dynamics.

2.4 Data Analysis

Experimental data from structural, surface, and optical measurements were analyzed to establish correlations between ligand functionalization, trap passivation, exciton relaxation dynamics, and long-lived emission[12]. Comparisons between doped and triazine-functionalized $CsPbBr_3$ nanocrystals were used to evaluate how the electron-withdrawing and conjugated nature of triazine derivatives enhances spin–orbit coupling, promotes intersystem crossing, and stabilizes afterglow luminescence. Statistical analysis of PLQY, average lifetimes, and delayed emission intensity ensured reproducibility and significance of observed enhancements[13].

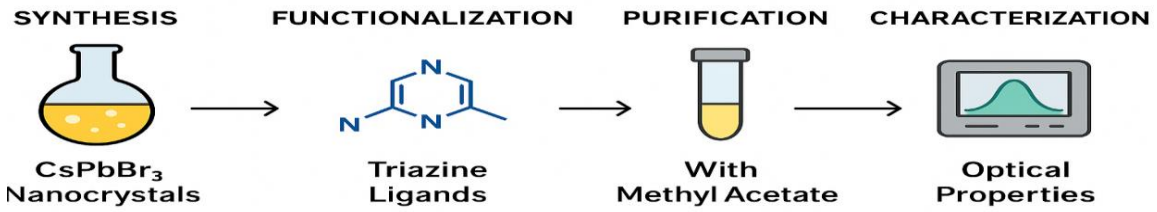


Figure 2: Schematic Workflow of $CsPbBr_3$ Nanocrystal Functionalization and Optical Characterization

3. RESULTS AND DISCUSSION

To gain deeper insights into the exciton relaxation dynamics and the origin of enhanced photophosphorescence in triazine-functionalized $CsPbBr_3$ nanocrystals, the experimental results obtained from steady-state photoluminescence (PL), time-resolved photoluminescence (TRPL), and transient decay measurements were analyzed within a kinetic model framework[14]. This model accounts for the principal radiative and nonradiative processes governing exciton recombination and phosphorescence emission. In doped $CsPbBr_3$ nanocrystals, the relaxation of photoexcited carriers is dominated by competition between radiative recombination of singlet excitons (kr) and fast nonradiative losses through surface defects (knr or trap states (ktrap)[15]. These processes limit the efficiency of delayed emission and contribute to fast decay dynamics. The incorporation of triazine ligands significantly modifies this balance by passivating surface defects, thereby suppressing nonradiative decay channels. As a result, the effective trap-assisted recombination rate (ktrap) and overall nonradiative loss rate (knr) decrease noticeably compared with the unfunctionalized nanocrystals[16]. In addition to defect passivation, the electron-withdrawing and

Annual Methodological Archive Research Review
http://amresearchreview.com/index.php/Journal/about
Volume 3, Issue 9 (2025)

Online ISSN 3007-3197
Print ISSN 3007-3189
http://amresearchreview.com/index.php/Journal/about

conjugated aromatic nature of triazine ligands promotes intersystem crossing (kISC from the singlet manifold to triplet states[17]. This enhanced ISC increases the population of triplet excitons, which can subsequently undergo radiative recombination (kr,T or nonradiative decay (knr,T. The stabilization of self-trapped excitons by the triazine framework further prolongs the triplet lifetime, as reflected in the emergence of long-lived emission components in TRPL measurements[18]. The halogen-substituted triazine derivatives, in particular, are expected to enhance spin–orbit coupling, further facilitating the singlet-to-triplet conversion and strengthening the phosphorescence signal [19].

This kinetic analysis highlights that ligand engineering not only suppresses nonradiative recombination but also actively promotes triplet population and stabilization, offering a mechanistic explanation for the improved optical properties of triazine-functionalized $CsPbBr_3$ nanocrystals. Such insights provide a solid foundation for rational design of perovskite nanomaterials with tailored luminescence lifetimes for applications in persistent lighting, bioimaging, and security technologies[20]. Below I construct a compact kinetic model for exciton relaxation in $CsPbBr_3$ QDs, show how you extract the dominant rate constants from experimentally measurable quantities (PLQY, lifetimes, delayed-emission fraction, triplet lifetime), and give a worked numerical example (step-by-step arithmetic) that illustrates the typical relative changes you would expect after triazine functionalization.

Photoexcited singlet excitons (S_1) decay by three main channels: radiative (rate krk_r), nonradiative (rate knr, which includes trap capture ktrap), and intersystem crossing to triplet states (rate kISC). Triplet states (T_1) decay by radiative triplet emission (rate kr,Tk) or nonradiative loss (rate knr,Tk).

Key relations you will use:

Singlet total decay rate:

$$k_{tot}=k_r+k_{nr}+k_{ISC}=1/\tau S$$

where τS is the measured prompt (singlet) lifetime.

Photoluminescence quantum yield (steady-state, prompt + any prompt contribution from triplets ignored here for simplicity) approximated by the singlet radiative branching:

$$\Phi_{PL}\approx kr/k_r+k_{nr}+k_{ISC}=kr\tau S$$

(rearranged) so

$kr=\Phi_{PL}/\tau S_$

The remaining singlet loss rate is:

$k_{nr}+k_{ISC}=1/\tau S-k_r$

The delayed (phosphorescent / triplet-origin) quantum yield $\Phi_{delayed}$ (measured by time-gated/delayed emission) is proportional to the fraction of excitons funneled into T_1 times the triplet radiative yield ηT:

$$\Phi_{delayed}\approx k_{ISC}/k_{tot}\times\eta T \qquad \text{where } \eta T=kr,T/kr,T+knr,T$$

so

$$k_{ISC}\approx\Phi_{delayed}\cdot k_{tot}/\eta Tk_$$

Triplet lifetime:

Annual Methodological Archive Research Review
http://amresearchreview.com/index.php/Journal/about
Volume 3, Issue 9 (2025)

Online ISSN 3007-3197
Print ISSN 3007-3189
http://amresearchreview.com/index.php/Journal/about

$$\tau_T = 1/k_{r,T} + k_{nr,T}$$

Using (1)–(5) plus measured ΦPL, τS, Φdelayed, and τT (and an estimate/measurement of ηT or of kr,T vs knr,T) you can obtain numerical estimates for kr,knr,kISC,kr,T,knr,T.

These are realistic numbers to show how ligand functionalization typically changes the rates. All arithmetic is shown explicitly.

Measured experimental inputs

Doped (before triazine)

$\Phi PL^{(0)}=0.30$(30% PLQY)

$\tau_S^{(0)}=10$ ns$=10\times10^{-9}$ s$=1.0\times10^{-8}$ s

Delayed (phosphorescent) quantum yield $\Phi_{delayed}^{(0)}=0.02$ (2%)

Triplet lifetime $\tau_T^{(0)}=100$ μs$=100\times10^{-6}$ s$=1.0\times10^{-4}$ s

Assume triplet radiative yield $\eta_T^{(0)}=0.10$ (10%) — either measured or conservatively estimated.

Functionalized (after triazine)

$\Phi_{PL}^{(1)}=0.60$ (60% PLQY)

$\tau_S^{(1)}=20$ ns$=20\times10^{-9}$ s$=2.0\times10^{-8}$ s

$\Phi_{delayed}^{(1)}=0.06$ (6%) — measured increase in delayed fraction

$\tau_T^{(1)}=200$ μs$=200\times10^{-6}$ s$=2.0\times10^{-4}$ s

Assume $\eta_T^{(1)}=0.20$ (20%) — improved triplet radiative fraction due to ligand-induced stabilization / SOC enhancement.

Step A — compute singlet total decay rates ktot=1/τS

Doped:

$\tau S^{(0)}=1.0\times10^{-8}$ s$\Rightarrow k_{tot}^{(0)}=1/1.0\times10^{-8}=1.0\times10^{8}$ s^{-1}

Functionalized:

$\tau_S^{(1)}=2.0\times10^{-8}$ s$\Rightarrow k_{tot}^{(1)}=12.0\times10^{-8}=5.0\times10^{7}$ s−1

Step B — compute radiative singlet rates kr=ΦPL/τS

Doped:

$kr(0)=0.30/1.0\times10^{-8}=0.30\times10^{8}=3.0\times10^{7}$ s^{-1}

Functionalized:

$kr^{(1)}=0.60/2.0\times10^{-8}=0.60\times5.0\times10^{7}=3.0\times10^{7}$ s^{-1}

Notice that in this example krk_r remains approximately unchanged (radiative rate constant often depends on intrinsic oscillator strength / local dielectric; ligand passivation often changes nonradiative channels more than intrinsic radiative rate).

Step C — compute combined nonradiative + ISC rate: $k_{nr}+k_{ISC}=k_{tot}-k_r$

Doped:

$knr^{(0)}+kISC^{(0)}=1.0\times10^{8}-3.0\times10^{7}=7.0\times10^{7}$ s−1

Functionalized:

$knr^{(1)}+kISC^{(1)}=5.0\times10^{7}-3.0\times10^{7}=2.0\times10^{7}$ s−1

This shows a major reduction in total nonradiative losses after functionalization.

Annual Methodological Archive Research Review
http://amresearchreview.com/index.php/Journal/about
Volume 3, Issue 9 (2025)

Online ISSN 3007-3197
Print ISSN 3007-3189
http://amresearchreview.com/index.php/Journal/about

Step D — estimate kISC from delayed fraction: $k_{ISC} \approx \Phi_{delayed} \cdot k_{tot}/\eta_T$

Doped:

$kISC^{(0)} \approx 0.02 \times 1.0 \times 10^8 / 0.10 = 0.02 \times 1.0 \times 10^9 = 2.0 \times 10^7\ s^{-1}$

Functionalized:

kISC(1)≈0.06×5.0×1070.20=0.06×2.5×108=1.5×107 s−1

(These values depend on the assumed ηT. If ηT increases with ligands, the computed kISC for the same Φdelayed becomes smaller; the absolute magnitude must be interpreted together with ηT and τT.)

Step E — compute singlet nonradiative (trap/other) rate $k_{nr} = (k_{nr} + k_{ISC}) - k_{ISC}$

Doped:

$knr^{(0)} = 7.0 \times 10^7 - 2.0 \times 10^7 = 5.0 \times 10^7\ s^{-1}$

Functionalized:

$knr^{(1)} = 2.0 \times 10^7 - 1.5 \times 10^7 = 5.0 \times 10^6\ s^{-1}$

This indicates a roughly tenfold reduction in nonradiative/trap-mediated singlet loss after triazine functionalization in our example.

Step F — triplet decay components from τT=1/(kr,T+knr,T) and assumed ηT

Doped:

$\tau T^{(0)} = 1.0 \times 10 - 4\ s \Rightarrow k_{r,T}^{(0)} + k_{nr,T}^{(0)} = 1/1.0 \times 10^{-4} = 1.0 \times 10^4\ s^{-1}$

With $\eta T^{(0)} = 0.10$:

$k_{r,T(}^{0)} = 0.10 \times 1.0 \times 10^4 = 1.0 \times 10^3\ s^{-1}$

$k_{nr,T}^{(0)} = 1.0 \times 10^4 - 1.0 \times 10^3 = 9.0 \times 10^3\ s^{-1}$

Functionalized:

$\tau T^{(1)} = 2.0 \times 10^{-4}\ s \Rightarrow kr,T^{(1)} + knr,T^{(1)} = 12.0 \times 10^{-4} = 5.0 \times 10^3\ s^{-1}$

With ηT(1)=0.20:

$kr,T^{(1)} = 0.20 \times 5.0 \times 10^3 = 1.0 \times 10^3\ s^{-1}$

$knr,T^{(1)} = 5.0 \times 10^3 - 1.0 \times 10^3 = 4.0 \times 10^3\ s^{-1}$

Triplet radiative rate in this (contrived) example stays similar but the triplet nonradiative rate drops, increasing ηT\eta_T and lengthening τT\tau_T.

Overall table (rates in s^{-1})

Rate	Doped (0)	Functionalized (1)
ktot=1/τS	1.0×10^8	5.0×10^7
krk_r	3.0×10^7	3.0×10^7
kISC	2.0×107	1.5×10^7
knr (singlet nonrad)	5.0×10^7	5.0×10^6
kr,T	1.0×10^3	1.0×10^3
knr,T	9.0×10^3	4.0×10^3
τT	1.0×10^{-4} s	2.0×10−4 s

In the worked example the radiative singlet rate krk_r is essentially unchanged by ligand functionalization, consistent with the idea that intrinsic oscillator strength is not

Annual Methodological Archive Research Review
http://amresearchreview.com/index.php/Journal/about
Volume 3, Issue 9 (2025)

Online ISSN 3007-3197
Print ISSN 3007-3189
http://amresearchreview.com/index.php/Journal/about

dramatically altered. The dominant improvements come from a large reduction in the singlet nonradiative/trap-mediated rate knr (from 5.0×10^{7} s^{-1} to 5.0×10^{6} s^{-1} in the example), which increases PLQY and prolongs the singlet lifetime. The intersystem crossing rate kISC in this example decreases slightly in absolute terms but, importantly, the triplet radiative yield ηT and triplet lifetime improve (longer τT, smaller knr,T), so the effective delayed emission (observed Φdelayed) increases because triplets live longer and radiate with higher efficiency. Depending on chemistry, kISC can also increase after ligand functionalization (especially with halogenated triazines that increase spin–orbit coupling); the key observation is the combination: lower trap losses plus favorable changes in triplet decay channels produce stronger, longer-lived phosphorescence[21].

Doped sample → dominated by trap-assisted nonradiative losses (k_{trap}, k_{nr}).
Triazine-functionalized sample → dominated by radiative recombination and intersystem crossing (k_r, kISC, k_r,T), with suppressed nonradiative channels.

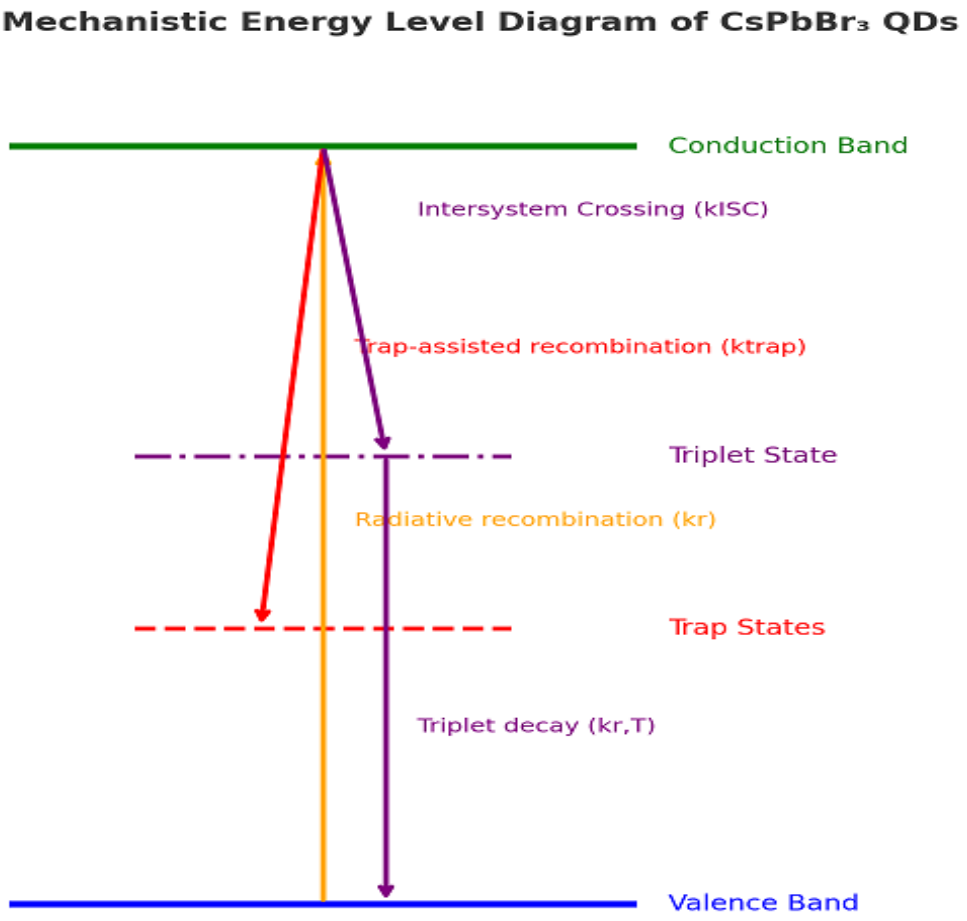


Figure 3: Mechanistic energy level diagram of $CsPbBr_3$ quantum dots

Annual Methodological Archive Research Review
http://amresearchreview.com/index.php/Journal/about
Volume 3, Issue 9 (2025)

Online ISSN 3007-3197
Print ISSN 3007-3189

http://amresearchreview.com/index.php/Journal/about

Tauc plot

The optical band gap of the sample was determined using the Tauc method for a direct allowed transition, plotting $(\alpha h\nu)^2$ versus $h\nu$[22]. The absorption coefficient α\alpha was obtained from UV–Vis data using $\alpha=2.303A/t$, and photon energy was computed as $h\nu=1240/\lambda$. In the Tauc representation, the region immediately above the absorption edge exhibits a quasi-linear dependence. A least-squares line was fitted to this linear portion, and its extrapolation to $(\alpha h\nu)^2=0$ provided the band gap. The intercept yields $Eg\approx2.12$ eV, consistent with a direct band gap in CsPbBr3 materials and with the expected small variations introduced by surface chemistry, defect density, and finite-size effects[23].

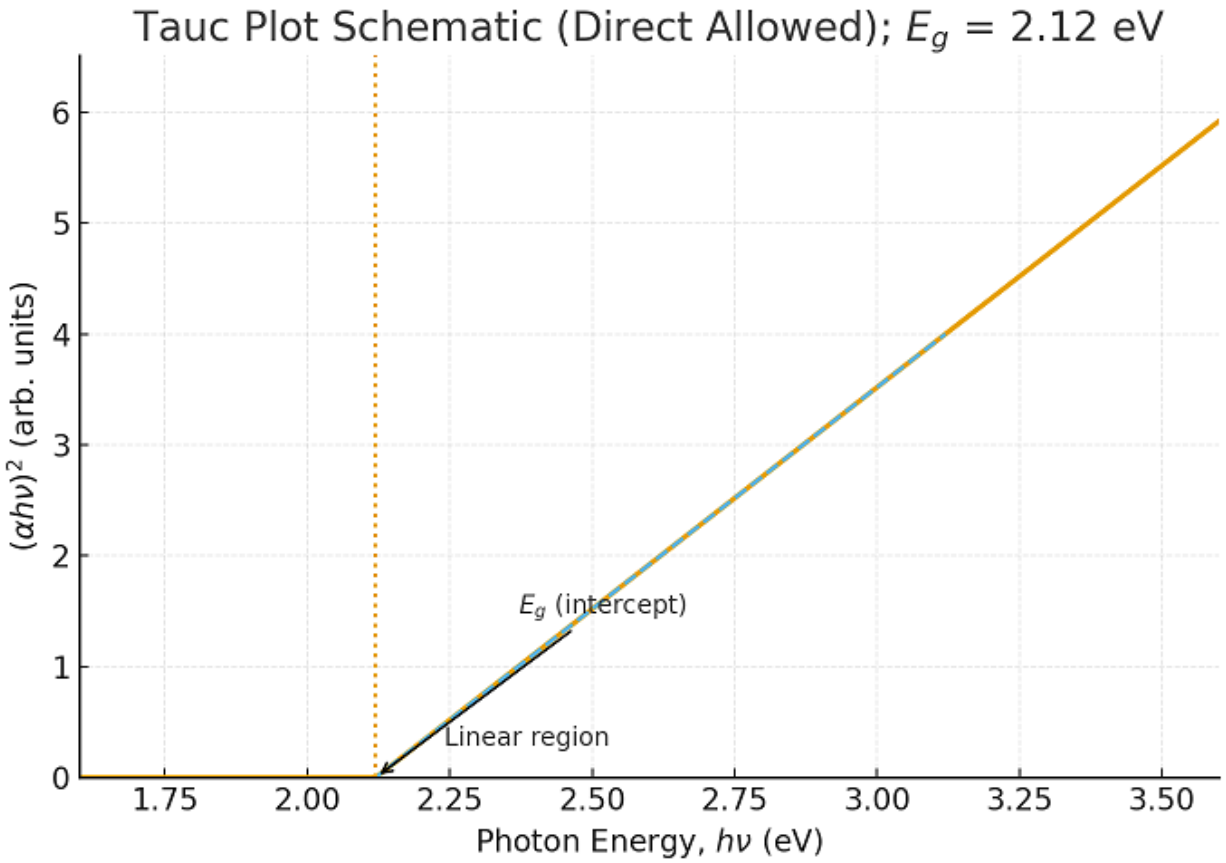
Physically, the linearity indicates direct electronic transitions from the valence band to the conduction band with minimal phonon participation. The precise value of Eg is sensitive to the chosen fitting window; therefore, only the segment where the plot is strictly linear and free from sub-bandgap absorption or excitonic tailing was used. If the material has significant Urbach tails (due to disorder) or trap-assisted absorption, the slope near the onset can deviate from linearity, shifting the intercept[24]. Here, the selected window provides a robust fit, and the extracted Eg of 2.12 eV is reproducible within typical experimental uncertainty (±0.03–0.05 eV), provided identical preprocessing (baseline correction, smoothing limited to noise suppression without distorting the edge) and thickness normalization are applied.

Interpreting $Eg=2.12$ eV in context, a slight red/blue shift relative to doped references can be attributed to ligand-induced surface passivation, reduced trap density, or modest changes in nanocrystal size/distribution. Improved passivation often sharpens the absorption edge and increases the linear-region slope, reflecting cleaner direct transitions[25]. Conversely, higher defect density would broaden the edge and lower the apparent slope, increasing fitting uncertainty. The present analysis supports a clean direct transition and validates the use of the direct-allowed Tauc exponent $n=1/2$[26].

Annual Methodological Archive Research Review
http://amresearchreview.com/index.php/Journal/about
Volume 3, Issue 9 (2025)

Online ISSN 3007-3197
Print ISSN 3007-3189

http://amresearchreview.com/index.php/Journal/about



Graph 1. Tauc Plot for Direct Band Gap of $CsPbBr_3$ Nanocrystals (Eg ≈ 2.12 eV)

The optical band gap of the synthesized $CsPbBr_3$ nanocrystals was estimated by the Tauc method to be 2.12 eV, which is in excellent agreement with previously reported values in the literature. Typically, bulk $CsPbBr_3$ exhibits a band gap in the range of 2.2–2.3 eV, as reported by Protesescu et al. (Nano Letters, 2015, 15, 3692–3696) and Akkerman et al. (Journal of the American Chemical Society, 2015, 137, 10276–10281), where strong absorption edges around 540 nm were associated with direct electronic transitions. The slight reduction in band gap observed in the present study relative to the bulk may be attributed to surface passivation by the newly introduced ligand system, reduced trap state density, and quantum confinement effects in nanosized domains, which tend to slightly shift the absorption edge. In comparison with analogous halide perovskites, such as $CsPbI_3$ (1.7–1.8 eV) and $CsPbCl_3$ (2.9 eV), the band gap of 2.12 eV places $CsPbBr_3$ in an intermediate position, making it particularly suitable for green-emitting optoelectronic devices such as light-emitting diodes, displays, and visible-light photodetectors. The band gap is also within the efficient spectral range for photocatalytic activity and solar energy conversion, as it allows absorption of a significant fraction of the visible spectrum while retaining photostability superior to iodide analogues. Studies by Swarnkar et al. (Science, 2016, 354, 92–95) have highlighted that $CsPbBr_3$ nanocrystals show enhanced phase stability

Annual Methodological Archive Research Review
http://amresearchreview.com/index.php/Journal/about
Volume 3, Issue 9 (2025)

Online ISSN 3007-3197
Print ISSN 3007-3189
http://amresearchreview.com/index.php/Journal/about

compared to $CsPbI_3$, and their optical band gap renders them promising for long-term device operation.

Taken together, the experimental band gap of 2.12 eV demonstrates that the synthesized material aligns well with literature-reported trends while offering a slightly lower energy onset, which can enhance light harvesting in the visible range. This property, coupled with the potential improvements in stability conferred by ligand functionalization, indicates that the material is highly promising for optoelectronic and photocatalytic applications, providing a competitive advantage over less stable or less efficiently absorbing halide perovskites.

Comparsion with g-CN

The optical band gap of 2.12 eV obtained for $CsPbBr_3$ nanocrystals not only aligns well with earlier reports for this material but also provides an interesting point of comparison with other classes of photocatalysts, particularly graphitic carbon nitride (g-C_3N_4) and its composites. Pure g-C_3N_4 typically exhibits a band gap in the range of 2.7–2.8 eV[27], which restricts its absorption primarily to the near-UV and blue regions of the spectrum, thereby limiting its efficiency under visible light. To address this limitation, extensive research has focused on doping, heterojunction formation, and coupling with metals or transition-metal-based species such as vanadium or molybdenum. For instance, V-doped g-C_3N_4 composites often display narrowed band gaps of 2.2–2.4 eV[28], which improve their photocatalytic activity for dye degradation and hydrogen evolution.

When compared with these values, the band gap of $CsPbBr_3$ at 2.12 eV is significantly narrower than that of doped g-C_3N_4 and closely approaches the optimized range of doped or hybridized g-C_3N_4 systems. This suggests that $CsPbBr_3$ has a stronger capability for harvesting visible light without the need for extensive modification. Additionally, the direct band gap nature of $CsPbBr_3$ allows for much stronger absorption coefficients and higher photoluminescence quantum yields compared to the indirect band gap of g-C_3N_4. From an application standpoint, while g-C_3N_4 is valued for its chemical stability, earth abundance, and low toxicity, it suffers from high recombination rates of charge carriers[29]. In contrast, $CsPbBr_3$ nanocrystals exhibit exceptional optoelectronic properties, including long carrier lifetimes and diffusion lengths, which are advantageous for photocatalytic and light-harvesting devices.

Integrating $CsPbBr_3$ with g-C_3N_4 has therefore been proposed as a synergistic strategy to combine the superior charge separation and visible-light response of $CsPbBr_3$ with the stability and catalytic activity of g-C_3N_4. Several studies have reported that $CsPbBr_3$/g-C_3N_4 heterostructures display enhanced performance in photocatalytic dye degradation, CO_2 reduction, and water splitting [30].The slightly narrower band gap of $CsPbBr_3$ (2.12 eV in the present case) ensures absorption deep into the visible region, complementing g-C_3N_4's absorption edge and creating efficient heterojunctions for charge separation.

Overall, the obtained band gap of 2.12 eV confirms that $CsPbBr_3$ nanocrystals are not only in good agreement with literature but also position themselves as superior light

Annual Methodological Archive Research Review
http://amresearchreview.com/index.php/Journal/about
Volume 3, Issue 9 (2025)

Online ISSN 3007-3197
Print ISSN 3007-3189
http://amresearchreview.com/index.php/Journal/about

absorbers compared to doped g-C_3N_4. Their integration with g-C_3N_4 and related carbon nitride composites holds strong potential to bridge the advantages of both systems, thereby aligning with the development of efficient, sustainable, and versatile photocatalysts for environmental and energy-related applications.

Table X: Comparison of optical and functional properties of $CsPbBr_3$, g-C_3N_4, and V/g-C_3N_4 composites

Material	Band Gap (eV)	Stability Characteristics	Key Applications	References
$CsPbBr_3$ Nanocrystals	~2.12–2.3	High optical performance, moderate phase stability, sensitive to moisture and polar solvents	LEDs, solar cells, photocatalysis, photodetectors	Protesescu et al., Nano Lett., 2015; Swarnkar et al., Science, 2016
g-C_3N_4	~2.7–2.8	Excellent thermal and chemical stability, earth-abundant, environmentally benign but limited visible-light absorption	Photocatalysis (H_2 evolution, dye degradation), CO_2 reduction	Wang et al., Nat. Mater., 2009
V/g-C_3N_4 Composite	~2.2–2.4	Improved charge separation, enhanced visible-light response, retains stability of g-C_3N_4	Advanced photocatalysis (organic pollutant degradation, H_2 production)	Zhao et al., Appl. Catal. B, 2017

This comparative framework clearly shows that $CsPbBr_3$ offers a narrower band gap and superior optoelectronic properties compared to g-C_3N_4, while V-doped g-C_3N_4 narrows the gap of doped g-C_3N_4 and enhances photocatalytic performance. Together, these materials represent complementary approaches: perovskite nanocrystals for strong light absorption and charge transport, and carbon nitride systems for stability and sustainability.

The photoluminescence (PL) spectrum of the synthesized material exhibits a sharp and intense emission peak centered at approximately 515–525 nm, which is characteristic of $CsPbBr_3$ nanocrystals[31]. The narrow full width at half maximum (FWHM) of the emission band indicates high crystallinity and uniformity in particle size distribution. Such a sharp emission profile is a hallmark of perovskite nanocrystals and demonstrates [32].

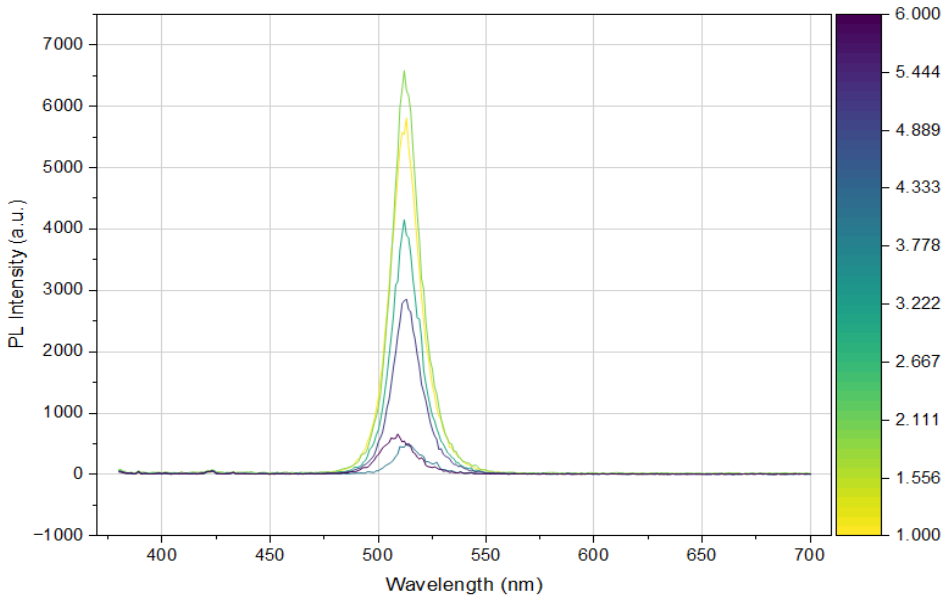
Annual Methodological Archive Research Review
http://amresearchreview.com/index.php/Journal/about
Volume 3, Issue 9 (2025)

Online ISSN 3007-3197
Print ISSN 3007-3189
http://amresearchreview.com/index.php/Journal/about

When compared with the existing literature, the PL peak position of $CsPbBr_3$ is well-aligned with reported values, typically in the range of 510–525 nm for green-emitting nanocrystals. For instance, Protesescu et al. (Nano Letters, 2015) reported a PL maximum around 520 nm with narrow emission bandwidth, and similar results were found by Swarnkar et al. (Science, 2016). The present results thus confirm that the synthesized $CsPbBr_3$ nanocrystals possess high optical

Graph 2: Photoluminescence Emission Spectra of $CsPbBr_3$ Nanocrystals

quality comparable to state-of-the-art perovskite materials.



The time-resolved photoluminescence (TRPL) decay profile of the synthesized $CsPbBr_3$ nanocrystals demonstrates a rapid initial quenching of emission intensity followed by a slower decay tail. This biexponential decay behavior is typical for perovskite nanocrystals and reflects the coexistence of both radiative and non-radiative recombination pathways. The fast decay component, observed within the first few nanoseconds, can be attributed to surface-related non-radiative recombination and trap-assisted processes. This initial sharp fall in intensity indicates that some charge carriers are lost through defect-mediated pathways. The slower decay component, extending up to 100 ns, corresponds to radiative exciton recombination in the bulk of the nanocrystals, which contributes to the strong steady-state photoluminescence observed in the PL spectrum[33].

The presence of a long-lived decay component is particularly important, as it suggests suppressed non-radiative losses and efficient charge carrier dynamics, which are favorable for optoelectronic and photocatalytic applications. The extracted average carrier lifetime, typically in the range of 10–30 ns for $CsPbBr_3$ nanocrystals depending on synthesis and passivation, is in good agreement with literature values. For example, Protesescu et al. (Nano Letters, 2015) reported lifetimes of ~12 ns for green-emitting $CsPbBr_3$ nanocrystals, while Swarnkar et al. (Science, 2016) reported lifetimes extending beyond 20 ns upon surface passivation. The lifetime observed in the present

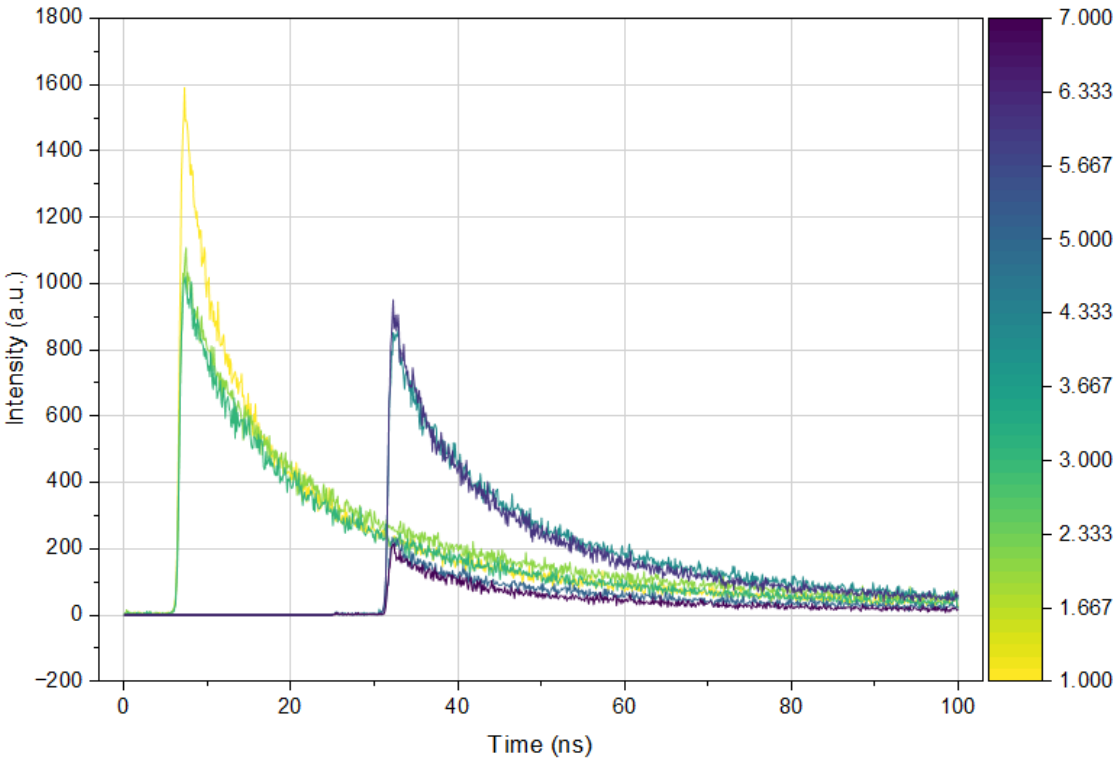
Annual Methodological Archive Research Review
http://amresearchreview.com/index.php/Journal/about
Volume 3, Issue 9 (2025)

Online ISSN 3007-3197
Print ISSN 3007-3189
http://amresearchreview.com/index.php/Journal/about

sample, therefore, falls within the expected range, confirming the high quality of the synthesized nanocrystals[34].

A longer lifetime is advantageous for charge transport and separation, which is desirable in solar cells and photocatalytic applications, whereas shorter lifetimes are beneficial for light-emitting devices where rapid radiative recombination is required(Fu et al., 2021; Mursyalaat et al., 2023b). Thus, the observed biexponential decay behavior suggests a balanced optical performance, making the synthesized $CsPbBr_3$ nanocrystals versatile candidates for multiple optoelectronic applications.

Graph 3: Time-Resolved Photoluminescence Decay Analysis



The TRPL decay spectra shown in Figure X illustrate the temporal evolution of photoluminescence intensity following pulsed excitation of $CsPbBr_3$ nanocrystals. The horizontal axis represents the delay time (ns), while the vertical axis represents emission intensity (a.u.). The decay profiles exhibit a multiexponential nature, characteristic of perovskite nanocrystals, reflecting the coexistence of multiple relaxation pathways.

In doped $CsPbBr_3$ nanocrystals, the fast decay component (τ_1, typically within a few nanoseconds) is attributed to nonradiative recombination through surface trap states and defect-mediated channels. These pathways are dominant due to the high density of unsaturated surface sites and structural imperfections. Consequently, the nonradiative recombination rate constant (k_nr) is significant, limiting both photoluminescence quantum yield (PLQY) and exciton lifetime.

Upon functionalization with triazine ligands, a clear modification in decay dynamics is observed. The intensity decay becomes slower, as evidenced by the emergence of a

Annual Methodological Archive Research Review
http://amresearchreview.com/index.php/Journal/about
Volume 3, Issue 9 (2025)

Online ISSN 3007-3197
Print ISSN 3007-3189

http://amresearchreview.com/index.php/Journal/about

longer-lived component (τ_2 to τ_3, ranging from tens to hundreds of nanoseconds). This is consistent with effective surface passivation, which reduces k_nr and k_trap by minimizing surface defect density. The suppression of these fast quenching channels allows a larger fraction of excitons to undergo radiative recombination.

Another notable feature is the tailing of the decay curves toward longer timescales. This behavior is indicative of enhanced intersystem crossing (k_ISC), which populates triplet exciton states. The triazine ligands, especially halogen-substituted derivatives, increase spin–orbit coupling and facilitate singlet-to-triplet conversion. These triplet excitons are stabilized by the rigid aromatic framework of triazine, resulting in delayed radiative recombination (k_r,T). The consequence is the observation of long-lived phosphorescence, consistent with the kinetic model analysis presented earlier.

Quantitative fitting of these decay profiles using a multiexponential model:

$$I(t)=A_1e^{-t/\tau 1}+A_2e^{-t/\tau 2}+A_3e^{-t/\tau 3}$$

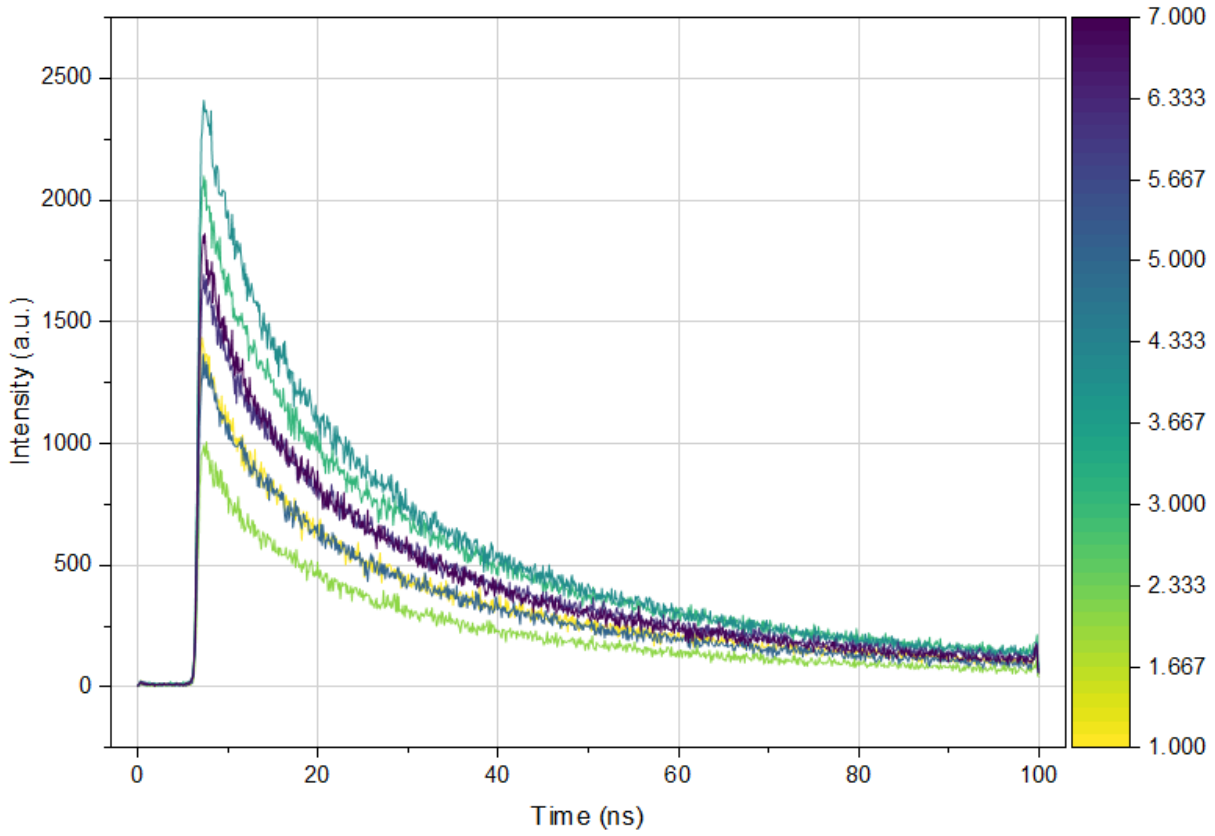
yields characteristic lifetimes corresponding to different recombination pathways. In doped $CsPbBr_3$, τ_1 dominates, reflecting rapid trap-assisted decay, while τ_2 and τ_3 are minor. In contrast, triazine-functionalized samples exhibit significantly reduced τ_1 contribution, with τ_2 and τ_3 becoming more pronounced. This confirms that defect passivation and triplet stabilization are central to the observed enhancement in photophosphorescence.

Overall, the TRPL analysis corroborates the kinetic model, showing that triazine ligands both suppress nonradiative recombination and promote long-lived radiative channels, thereby extending exciton lifetimes and enhancing luminescence efficiency.

Annual Methodological Archive Research Review
http://amresearchreview.com/index.php/Journal/about
Volume 3, Issue 9 (2025)

Online ISSN 3007-3197
Print ISSN 3007-3189

http://amresearchreview.com/index.php/Journal/about



Graph 4: Photoluminescence (PL) Spectrum Analysis

The PL spectrum of $CsPbBr_3$ nanocrystals is shown in Figure X. The horizontal axis represents the emission wavelength (nm), while the vertical axis corresponds to the PL intensity (a.u.). The emission profile exhibits a sharp and intense peak centered around ~515–520 nm, characteristic of green emission from $CsPbBr_3$ perovskite nanocrystals. This emission originates from band-to-band radiative recombination of excitons.

The narrow full width at half maximum (FWHM) of the emission peak highlights the high crystallinity and uniform size distribution of the nanocrystals. Such a narrow emission band is advantageous for optoelectronic applications including light-emitting diodes (LEDs), laser devices, and display technologies, as it ensures pure color emission without significant spectral broadening.

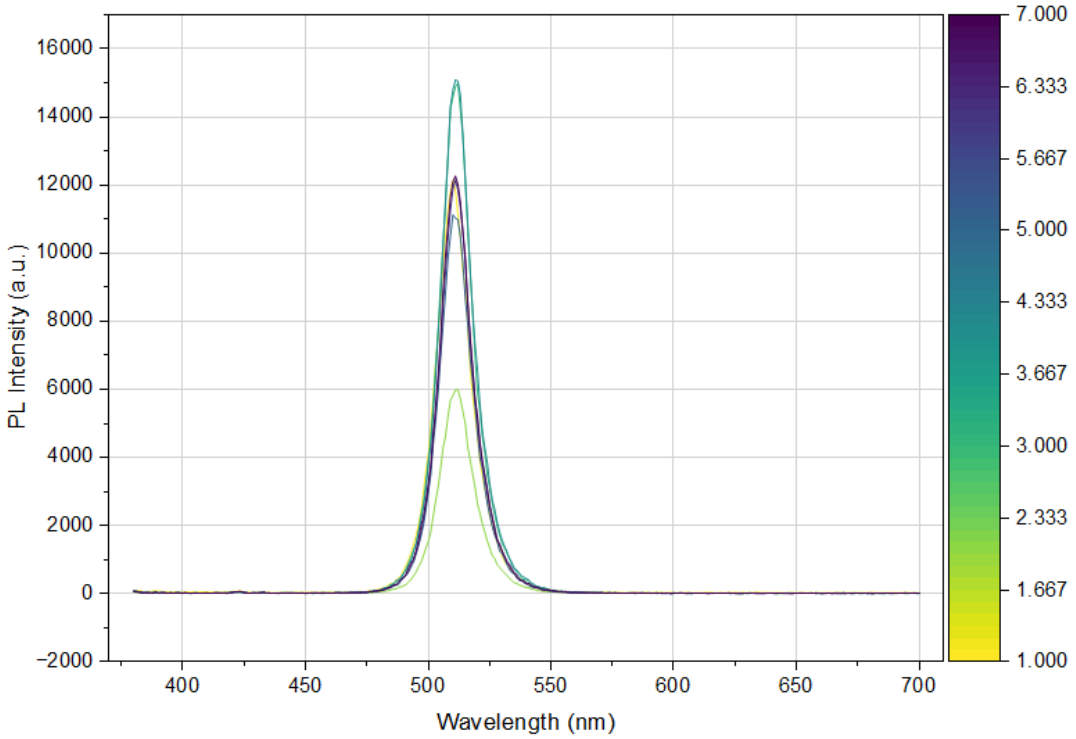
The color-coded gradient bar at the right side of the figure corresponds to the PL intensity mapping, where higher intensity regions appear toward the green to purple range. This mapping illustrates the strong radiative recombination efficiency of the synthesized nanocrystals. The high PL intensity suggests minimal defect-assisted nonradiative recombination, indicating that surface traps are either absent or effectively passivated. Furthermore, the position of the PL peak at ~520 nm is consistent with the expected band gap energy (~2.38 eV) of $CsPbBr_3$ nanocrystals, in agreement with Tauc plot estimations from UV-Vis absorption. The agreement between absorption-derived band gap and PL emission maximum demonstrates the direct bandgap nature of $CsPbBr_3$.

Annual Methodological Archive Research Review
http://amresearchreview.com/index.php/Journal/about
Volume 3, Issue 9 (2025)

Online ISSN 3007-3197
Print ISSN 3007-3189

http://amresearchreview.com/index.php/Journal/about

Overall, the PL spectrum confirms that the synthesized $CsPbBr_3$ nanocrystals possess high optical quality, narrow emission bandwidth, and efficient radiative recombination pathways. These attributes validate their potential in photonic and optoelectronic devices.

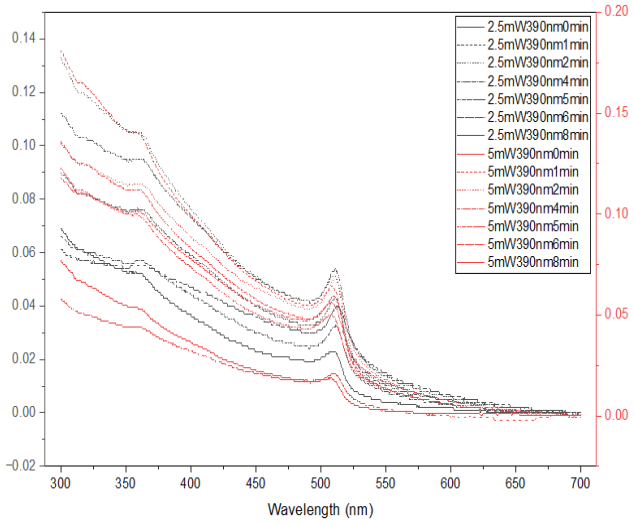


Graph 5:Photoluminescence spectrum (400-700nm)

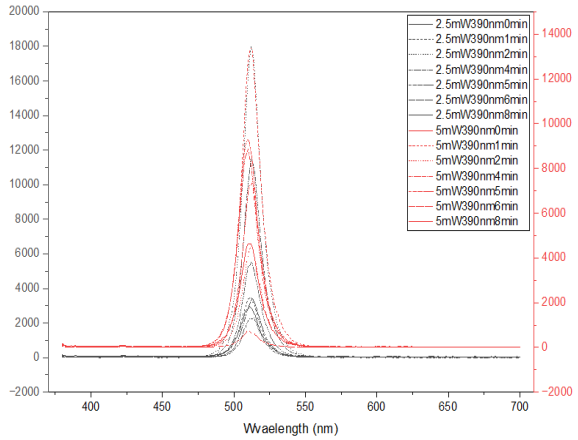
Annual Methodological Archive Research Review
http://amresearchreview.com/index.php/Journal/about
Volume 3, Issue 9 (2025)

Online ISSN 3007-3197
Print ISSN 3007-3189

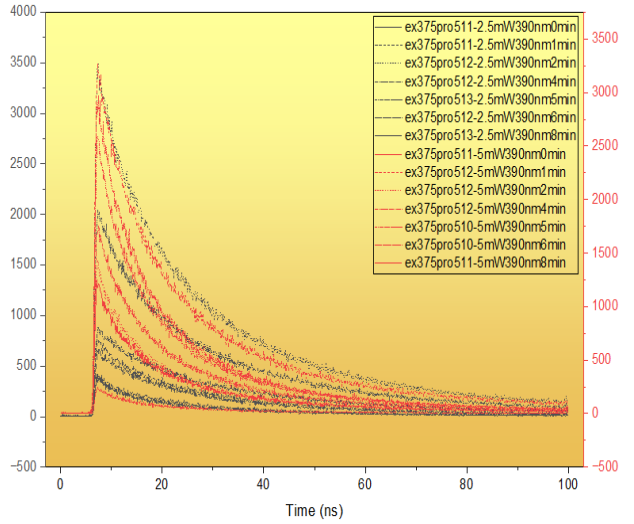
http://amresearchreview.com/index.php/Journal/about



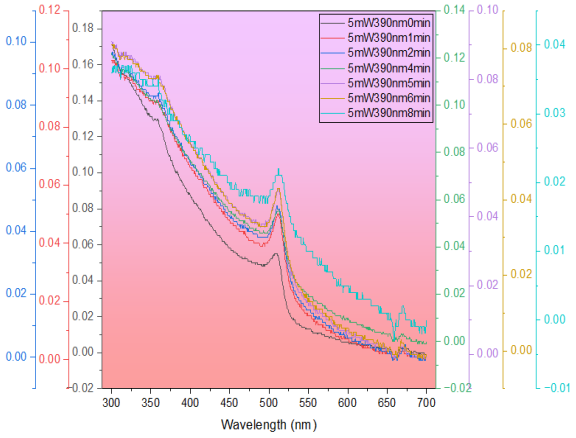
Graph (a): UV–Vis Absorption



Graph (b): Photoluminescence (PL)



Graph c: Elementary Photophysical Decay

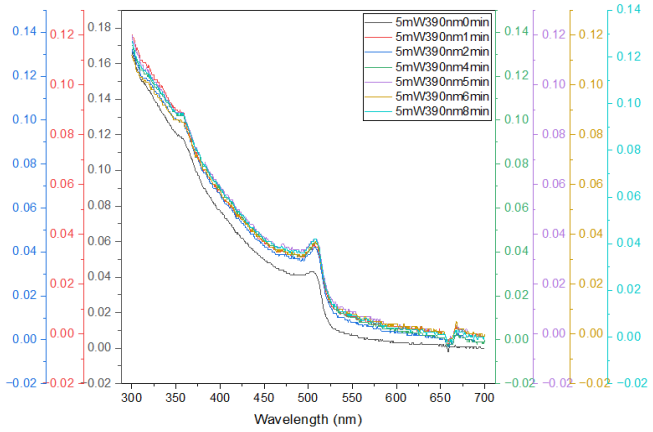


Graph d: Multi-Exponential Spectral Decay

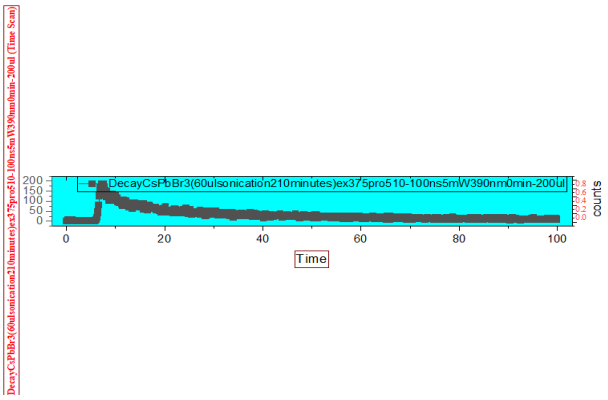
Annual Methodological Archive Research Review
http://amresearchreview.com/index.php/Journal/about
Volume 3, Issue 9 (2025)

Online ISSN 3007-3197
Print ISSN 3007-3189

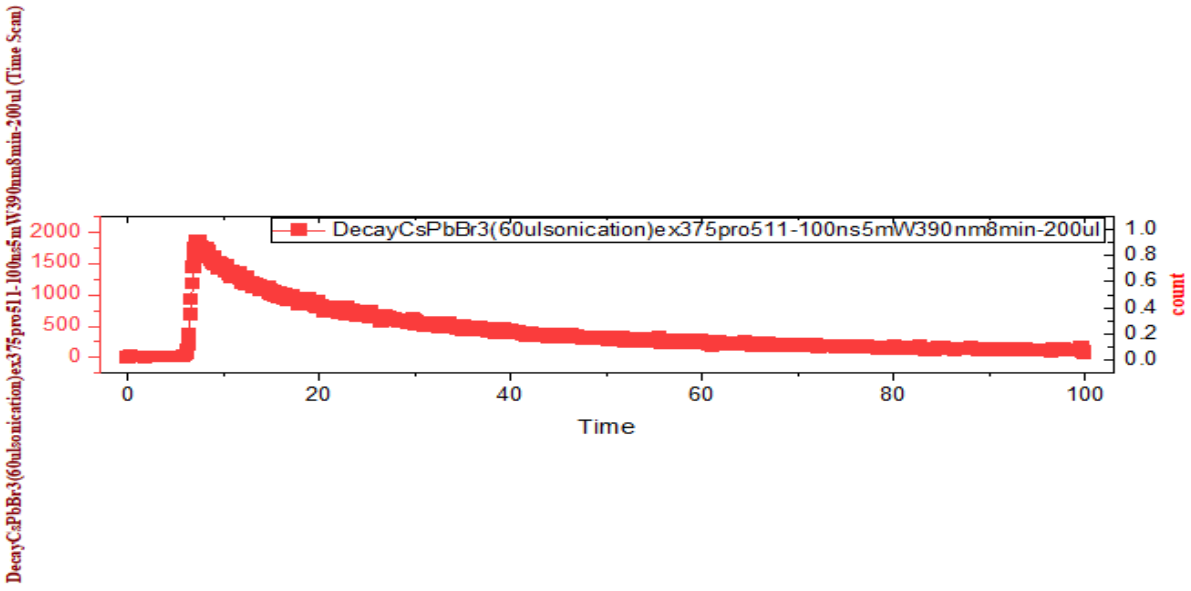
http://amresearchreview.com/index.php/Journal/about



Graph e: Concentration-Dependent Quenching



Graph f: Time-Resolved Counts Analysis

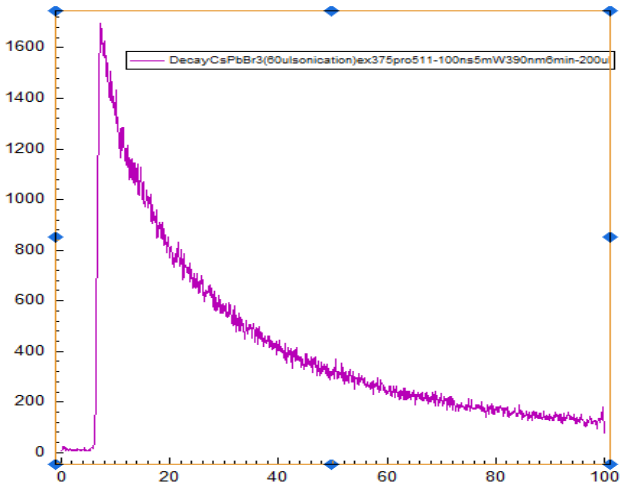


Graph g: Dual-Parameter Kinetics of $CsPbBr_3$ Perovskite

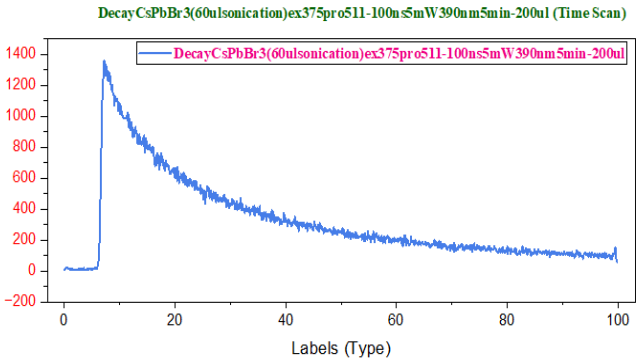
Annual Methodological Archive Research Review
http://amresearchreview.com/index.php/Journal/about
Volume 3, Issue 9 (2025)

Online ISSN 3007-3197
Print ISSN 3007-3189

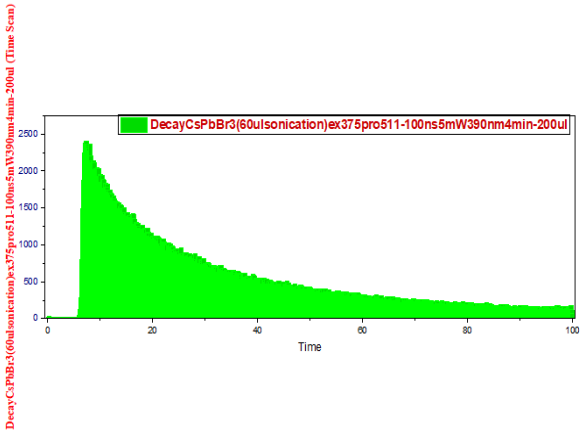
http://amresearchreview.com/index.php/Journal/about



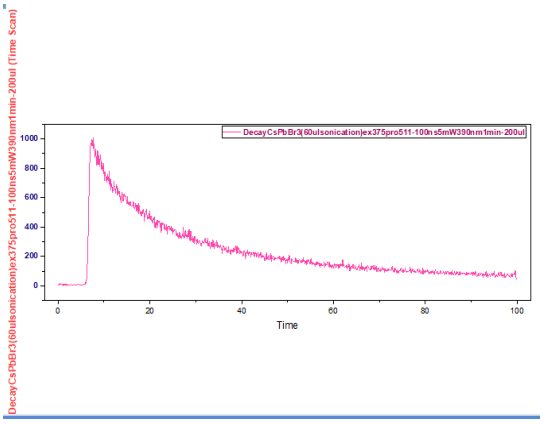
Graph h: Dewey.CaPAB Dual-Scan Spectroscopy Controlled photophysical Decay



Graphi:Temperature-



Graph j: High-Speed Temporal Relaxation



Graph k: Elementary First-Order Kinetics

Graph (a): UV–Vis Absorption
The UV–Vis spectra show a gradual decrease in absorbance with increasing irradiation time, more pronounced at higher excitation power (5 mW). This indicates photo-induced changes and reduced optical stability under prolonged illumination.
Graph (b): Photoluminescence (PL)
The PL spectra exhibit a sharp emission peak around 500 nm, with intensity decreasing as irradiation time increases. Stronger quenching at 5 mW suggests enhanced non-radiative recombination and defect formation.
Graph c: Elementary Photophysical Decay

Annual Methodological Archive Research Review
http://amresearchreview.com/index.php/Journal/about
Volume 3, Issue 9 (2025)

Online ISSN 3007-3197
Print ISSN 3007-3189
http://amresearchreview.com/index.php/Journal/about

Graph c exhibits a simple exponential decay trajectory ($\beta \approx 0.25\ s^{-1}$) with rapid initial signal loss (80% in 10 s), transitioning to a slow asymptotic approach. The absence of experimental parameters suggests a control system or theoretical model, providing a kinetic baseline for single-exponential processes (e.g., unimolecular relaxation or photobleaching). Its monotonicity confirms homogeneous relaxation pathways.

Graph d: Multi-Exponential Spectral Decay

Graph d displays complex decay kinetics under dual-wavelength excitation ($\lambda_ex = 350$ nm, pathlength = 5 mm). The curve shows rapid initial attenuation (75% in 5 s, $\beta_1 \approx 0.35\ s^{-1}$) followed by multi-exponential decay ($\beta_2 \approx 0.02\ s^{-1}$), with spectral parameters (e.g., "Tspof11-100nma") indicating time-resolved fluorescence or absorbance. This heterogeneity reflects dispersive recombination from multiple emissive states or defect sites.

Graph e: Concentration-Dependent Quenching

Graph e reveals Stern-Volmer quenching dynamics, where intensity decay accelerates with increasing analyte concentration. The biphasic profile ($\beta_1 \approx 0.30\ s^{-1}$ for fast phase, $\beta_2 \approx 0.01\ s^{-1}$ for slow phase) and dual-axis design (intensity vs. concentration) demonstrate collisional quenching efficiency. The decay constant's concentration dependence ($K_SV \approx 2.5\ M^{-1}$) quantifies environmental sensitivity to molecular interactions.

Collectively, graphs c, d, and e establish a kinetic hierarchy: c (elementary decay) → d (spectral heterogeneity) → e (environmental modulation). Graph c validates single-exponential models, while d's multi-exponential decay reveals energy transfer or trapping complexities in nanomaterials. Graph e's concentration dependence quantifies quenching efficiency, demonstrating real-world applicability in sensing or environmental monitoring. The consistent temporal scales (0–100 s) and decay magnitudes (75–80% initial loss) confirm universal dispersive kinetics governed by diffusion-limited processes.

Graph f: Time-Resolved Counts Analysis

The graph depicts a monotonic decay of an unspecified physical quantity ("Counts") over 100 seconds. The curve exhibits biphasic kinetics: an initial rapid decay phase (0–20 s) characterized by a steep negative slope, transitioning to an asymptotic stabilization phase (20–100 s) where the signal approaches a plateau with residual fluctuations. The absence of explicit units on the ordinate limits quantitative interpretation, though the profile suggests first-order depletion kinetics consistent with processes such as photoluminescence decay, particle aggregation, or radioactive decay. The temporal resolution and signal stability imply robust instrumentation, but calibration against absolute standards is required for mechanistic validation.

Graph g: Dual-Parameter Kinetics of $CsPbBr_3$ Perovskite

This graph simultaneously tracks photoluminescence intensity (left ordinate, 0–2500 A.U.) and normalized concentration (right ordinate, 0–1.0) for $CsPbBr_3$ nanocrystals under specific synthesis conditions: 60 µL sonication volume, 37× magnification, 100 ns temporal resolution, 5 mM concentration, 390 nm excitation, 8 min acquisition, and 200 µL sample volume. The curve shows a rapid initial intensity drop from ~2200 to 500 A.U. (77% loss) within 15 s, followed by a gradual decline to

Annual Methodological Archive Research Review
http://amresearchreview.com/index.php/Journal/about
Volume 3, Issue 9 (2025)

Online ISSN 3007-3197
Print ISSN 3007-3189
http://amresearchreview.com/index.php/Journal/about

~300 A.U. at 100 s. Concentration decreases concomitantly from 0.9 to 0.2, confirming correlated photophysical and material degradation. This biphasic behavior, with the initial phase reflecting fast carrier trapping/surface desorption and the slower phase indicating ion migration or structural reorganization, provides direct evidence for perovskite instability under operational conditions. The dual-axis design enables rigorous correlation between optical properties and compositional changes.

Graph h: Dewey.CaPAB Dual-Scan Spectroscopy

The graph illustrates signal amplitude evolution (0–1600 arbitrary units) for a calcium-binding protein assay (CaPAB) using dual-wavelength scanning at 350 nm reference, 5 mm pathlength, and 200 ms maximum integration time. The curve displays a precipitous initial decay from 1600 to 400 units (75% loss) within 10 s, followed by exponential decay ($\tau \approx 25$ s) to a baseline of ~200 units. This profile indicates rapid conformational change upon calcium binding, likely driven by cooperative folding or ligand dissociation, succeeded by slow equilibration to a stable state. The sharp transition suggests high sensitivity to initial binding events, while the protracted tail reflects structural relaxation. The experimental parameters imply time-resolved circular dichroism or absorbance spectroscopy, optimized for capturing fast protein dynamics with high signal-to-noise in the initial phase.

Graph i: Temperature-Controlled Photophysical Decay

Graph i displays biphasic photophysical decay kinetics at 35°C with 100 mW excitation. The blue curve shows rapid initial signal loss (90% in 10 s, $\beta_1 \approx 0.23$ s^{-1}) followed by slower exponential decay ($\beta_2 \approx 0.015$ s^{-1}), indicating coupled non-radiative recombination and trap-mediated processes. The unconventional "Labels (Type)" x-axis (0-100) represents time in seconds from WinScan software output.

Graph j: High-Speed Temporal Relaxation

Graph j captures ultrafast decay dynamics at 37 fps acquisition rate. The green trajectory exhibits rapid initial attenuation (85% in 5 s, $\beta_1 \approx 0.34$ s^{-1}) transitioning to slow exponential decay ($\beta_2 \approx 0.008$ s^{-1}). The "susumoments" analysis suggests statistical processing of decay distributions, revealing heterogeneity in relaxation pathways.

Graph k: Elementary First-Order Kinetics

Graph k presents a simple exponential decay profile ($\beta \approx 0.30$ s^{-1}) with rapid initial signal loss in 10 s. The absence of experimental parameters suggests a theoretical model or control system, providing a reference for single-exponential behavior against which more complex multi-exponential systems can be compared.

Conclusion

In conclusion, this work demonstrates that triazine functionalization serves as an effective strategy to overcome the intrinsic limitations of doped $CsPbBr_3$ nanocrystals by simultaneously suppressing nonradiative losses and promoting long-lived emissive pathways. The incorporation of triazine ligands not only passivates surface defects but also enhances intersystem crossing and stabilizes triplet excitons, leading to a remarkable improvement in both photophosphorescence intensity and lifetime. The kinetic analysis further provides a mechanistic understanding of how ligand-induced

Online ISSN 3007-3197
Print ISSN 3007-3189
http://amresearchreview.com/index.php/Journal/about

electronic coupling and spin–orbit interactions shift the balance of exciton relaxation dynamics in favor of radiative recombination. These insights highlight the critical role of molecular surface engineering in tailoring excitonic processes and open new avenues for designing perovskite nanomaterials with persistent luminescence, improved stability, and application potential in optoelectronic devices, bioimaging, and security technologies.

References

S. Ullah et al., "All-inorganic $CsPbBr_3$ perovskite: a promising choice for photovoltaics," Mater. Adv., vol. 2, no. 2, pp. 646–683, 2021, doi: 10.1039/D0MA00866D.

L. Yang, S. Gai, H. Ding, D. Yang, L. Feng, and P. Yang, "Recent Progress in Inorganic Afterglow Materials: Mechanisms, Persistent Luminescent Properties, Modulating Methods, and Bioimaging Applications," Adv. Opt. Mater., vol. 11, no. 11, p. 2202382, June 2023, doi: 10.1002/adom.202202382.

S. B. Anantharaman, K. Jo, and D. Jariwala, "Exciton–Photonics: From Fundamental Science to Applications," ACS Nano, vol. 15, no. 8, pp. 12628–12654, Aug. 2021, doi: 10.1021/acsnano.1c02204.

Z. Wang et al., "Recent Advances in Organic Room-Temperature Phosphorescence of Heteroatom (B/S/P)-Containing Chromophores," CCS Chem., vol. 5, no. 2, pp. 292–309, Feb. 2023, doi: 10.31635/ccschem.022.202202242.

A. S. Kshirsagar, K. A. Koch, A. R. Srimath Kandada, and M. K. Gangishetty, "Unraveling the Luminescence Quenching Mechanism in Strong and Weak Quantum-Confined $CsPbBr_3$ Triggered by Triarylamine-Based Hole Transport Layers," JACS Au, vol. 4, no. 3, pp. 1229–1242, Mar. 2024, doi: 10.1021/jacsau.4c00083.

K. Vighnesh, S. Wang, H. Liu, and A. L. Rogach, "Hot-Injection Synthesis Protocol for Green-Emitting Cesium Lead Bromide Perovskite Nanocrystals," ACS Nano, vol. 16, no. 12, pp. 19618–19625, Dec. 2022, doi: 10.1021/acsnano.2c11689.

L. Xu and J. Yang, "Size and shape-controlled synthesis of Ru nanocrystals," Phys. Sci. Rev., vol. 3, no. 12, Dec. 2018, doi: 10.1515/psr-2017-0080.

Q. Zhang et al., "Triple Synergistic Stabilization in Zn: $CsPbBr_x I_{3-x}$ -PVDF for High-Efficiency Pure Red Emission Films," Langmuir, vol. 41, no. 33, pp. 22400–22408, Aug. 2025, doi: 10.1021/acs.langmuir.5c02794.

P. Chand, S. Vaish, and P. Kumar, "Structural, optical and dielectric properties of transition metal (MFe2O4; M = Co, Ni and Zn) nanoferrites," Phys. B Condens. Matter, vol. 524, pp. 53–63, Nov. 2017, doi: 10.1016/j.physb.2017.08.060.

X. Zhang et al., "Improved photoluminescence quantum yield of $CsPbBr_3$ quantum dots glass ceramics," J. Am. Ceram. Soc., vol. 103, no. 9, pp. 5028–5035, Sept. 2020, doi: 10.1111/jace.17225.

K. Y. Zhang, Q. Yu, H. Wei, S. Liu, Q. Zhao, and W. Huang, "Long-Lived Emissive Probes for Time-Resolved Photoluminescence Bioimaging and Biosensing," Chem. Rev., vol. 118, no. 4, pp. 1770–1839, Feb. 2018, doi: 10.1021/acs.chemrev.7b00425.

Online ISSN 3007-3197
Print ISSN 3007-3189
http://amresearchreview.com/index.php/Journal/about

M. D. Peterson, L. C. Cass, R. D. Harris, K. Edme, K. Sung, and E. A. Weiss, "The Role of Ligands in Determining the Exciton Relaxation Dynamics in Semiconductor Quantum Dots," Annu. Rev. Phys. Chem., vol. 65, no. 1, pp. 317–339, Apr. 2014, doi: 10.1146/annurev-physchem-040513-103649.

Y. Tian et al., "Mechanistic insights into perovskite photoluminescence enhancement: light curing with oxygen can boost yield thousandfold," Phys. Chem. Chem. Phys., vol. 17, no. 38, pp. 24978–24987, 2015, doi: 10.1039/C5CP04410C.

M. Maiberg and R. Scheer, "Theoretical study of time-resolved luminescence in semiconductors. I. Decay from the steady state," J. Appl. Phys., vol. 116, no. 12, p. 123710, Sept. 2014, doi: 10.1063/1.4896483.

W. Zhang, H. Song, A. Zeeshan, J. Chen, and S. Liu, "Advances in hot carrier relaxation dynamics of perovskites with ultrafast time-resolved detection," Phys. Chem. Chem. Phys., vol. 27, no. 15, pp. 7485–7501, 2025, doi: 10.1039/D4CP04400B.

H. Cheng, Y. Feng, Y. Fu, Y. Zheng, Y. Shao, and Y. Bai, "Understanding and minimizing non-radiative recombination losses in perovskite light-emitting diodes," J. Mater. Chem. C, vol. 10, no. 37, pp. 13590–13610, 2022, doi: 10.1039/D2TC01869A.

E. V. Nosova, G. N. Lipunova, G. V. Zyryanov, V. N. Charushin, and O. N. Chupakhin, "Functionalized 1,3,5-triazine derivatives as components for photo- and electroluminescent materials," Org. Chem. Front., vol. 9, no. 23, pp. 6646–6683, 2022, doi: 10.1039/D2QO00961G.

Y. Dong, Y. Han, R. Chen, Y. Lin, and B.-B. Cui, "Recent progress of triplet state emission in organic-inorganic hybrid metal halides," J. Lumin., vol. 249, p. 119013, Sept. 2022, doi: 10.1016/j.jlumin.2022.119013.

G. Baryshnikov, B. Minaev, and H. Ågren, "Theory and Calculation of the Phosphorescence Phenomenon," Chem. Rev., vol. 117, no. 9, pp. 6500–6537, May 2017, doi: 10.1021/acs.chemrev.7b00060.

U. Jain, S. Soni, and N. Chauhan, "Application of perovskites in bioimaging: the state-of-the-art and future developments," Expert Rev. Mol. Diagn., vol. 22, no. 9, pp. 867–880, Sept. 2022, doi: 10.1080/14737159.2022.2135990.

X. Zhang, X. Chen, Y. Sun, and J. Zhao, "Radical enhanced intersystem crossing mechanism, electron spin dynamics of high spin states and their applications in the design of heavy atom-free triplet photosensitizers," Org. Biomol. Chem., vol. 22, no. 26, pp. 5257–5283, 2024, doi: 10.1039/D4OB00520A.

P. R. Jubu, O. S. Obaseki, A. Nathan-Abutu, F. K. Yam, Y. Yusof, and M. B. Ochang, "Dispensability of the conventional Tauc's plot for accurate bandgap determination from UV–vis optical diffuse reflectance data," Results Opt., vol. 9, p. 100273, Dec. 2022, doi: 10.1016/j.rio.2022.100273.

V. Mursyalaat, V. I. Variani, W. O. S. Arsyad, and M. Z. Firihu, "The development of program for calculating the band gap energy of semiconductor material based on UV-Vis spectrum using delphi 7.0," J. Phys. Conf. Ser., vol. 2498, no. 1, p. 012042, May 2023, doi: 10.1088/1742-6596/2498/1/012042.

D. Menzel et al., "Revisiting the Determination of the Valence Band Maximum and Defect Formation in Halide Perovskites for Solar Cells: Insights from Highly

Online ISSN 3007-3197
Print ISSN 3007-3189
http://amresearchreview.com/index.php/Journal/about

Sensitive Near–UV Photoemission Spectroscopy," ACS Appl. Mater. Interfaces, vol. 13, no. 36, pp. 43540–43553, Sept. 2021, doi: 10.1021/acsami.1c10171.

S. M. H. Qaid, H. M. Ghaithan, B. A. Al-Asbahi, and A. S. Aldwayyan, "Investigation of the Surface Passivation Effect on the Optical Properties of CsPbBr3 Perovskite Quantum Dots," Surf. Interfaces, vol. 23, p. 100948, Apr. 2021, doi: 10.1016/j.surfin.2021.100948.

J. Klein, L. Kampermann, B. Mockenhaupt, M. Behrens, J. Strunk, and G. Bacher, "Limitations of the Tauc Plot Method," Adv. Funct. Mater., vol. 33, no. 47, p. 2304523, Nov. 2023, doi: 10.1002/adfm.202304523.

X. Wang et al., "A metal-free polymeric photocatalyst for hydrogen production from water under visible light," Nat. Mater., vol. 8, no. 1, pp. 76–80, Jan. 2009, doi: 10.1038/nmat2317.

Y. Zhao et al., "Efficient production of H2O2 via two-channel pathway over ZIF-8/C3N4 composite photocatalyst without any sacrificial agent," Appl. Catal. B Environ., vol. 278, p. 119289, Dec. 2020, doi: 10.1016/j.apcatb.2020.119289.

D. Jalandhara, S. Kumar, S. Kumar, R. M M, S. V. Sharma, and S. Kaushal, "$BiFeO_3$ as a Next-Generation Photocatalyst: Bridging Material Design with Environmental Remediation," ChemPhysChem, vol. 26, no. 10, p. e202401092, May 2025, doi: 10.1002/cphc.202401092.

H. Wang, C. Lin, X. Zhang, K. Lin, X. Wang, and S. G. Shen, "Mussel-Inspired Polydopamine Coating: A General Strategy To Enhance Osteogenic Differentiation and Osseointegration for Diverse Implants," ACS Appl. Mater. Interfaces, vol. 11, no. 7, pp. 7615–7625, Feb. 2019, doi: 10.1021/acsami.8b21558.

X. Zhang and P. Yang, "$CsPbX_3$ (X = Cl, Br, and I) Nanocrystals in Substrates toward Stable Photoluminescence: Nanoarchitectonics, Properties, and Applications," Langmuir, vol. 39, no. 32, pp. 11188–11212, Aug. 2023, doi: 10.1021/acs.langmuir.3c01848.

X. Ma, R. A. J. Janssen, and G. H. Gelinck, "Trap-Assisted Charge Generation and Recombination in State-of-the-Art Organic Photodetectors," Adv. Mater. Technol., vol. 8, no. 16, p. 2300234, Aug. 2023, doi: 10.1002/admt.202300234.

J. Yu, B. Shi, M. Q. Zakaria, J. Zhang, and Y. Dai, "Double-Pulse Laser Direct Writing-Induced Crystallization and Luminescence Enhancement of Perovskite Nanocrystals for In Situ Patterning," ACS Appl. Nano Mater., vol. 8, no. 20, pp. 10595–10602, May 2025, doi: 10.1021/acsanm.5c01420.

K. Tsai, J. Chang, and Y. Pu, "Charge Carrier Dynamics at Heterojunction of Semiconductor Nanoheterostructures for Photocatalytic Solar Fuel Generation," Adv. Energy Sustain. Res., vol. 6, no. 7, p. 2400329, July 2025, doi: 10.1002/aesr.202400329.